nature medicine

Parkinson's disease–associated mutant VPS35 causes mitochondrial dysfunction by recycling DLP1 complexes

Wenzhang Wang[1,9], Xinglong Wang[1,9], Hisashi Fujioka[2], Charles Hoppel[3,4], Alan L Whone[5], Maeve A Caldwell[6], Peter J Cullen[7], Jun Liu[8] & Xiongwei Zhu[1]

Mitochondrial dysfunction represents a critical step during the pathogenesis of Parkinson's disease (PD), and increasing evidence suggests abnormal mitochondrial dynamics and quality control as important underlying mechanisms. The *VPS35* gene, which encodes a key component of the membrane protein–recycling retromer complex, is the third autosomal-dominant gene associated with PD. However, how *VPS35* mutations lead to neurodegeneration remains unclear. Here we demonstrate that PD-associated *VPS35* mutations caused mitochondrial fragmentation and cell death in cultured neurons *in vitro,* in mouse substantia nigra neurons *in vivo* and in human fibroblasts from an individual with PD who has the *VPS35*^{D620N} mutation. *VPS35*-induced mitochondrial deficits and neuronal dysfunction could be prevented by inhibition of mitochondrial fission. VPS35 mutants showed increased interaction with dynamin-like protein (DLP) 1, which enhanced turnover of the mitochondrial DLP1 complexes via the mitochondria-derived vesicle–dependent trafficking of the complexes to lysosomes for degradation. Notably, oxidative stress increased the VPS35-DLP1 interaction, which we also found to be increased in the brains of sporadic PD cases. These results revealed a novel cellular mechanism for the involvement of VPS35 in mitochondrial fission, dysregulation of which is probably involved in the pathogenesis of familial, and possibly sporadic, PD.

© 2015 Nature America, Inc. All rights reserved.

Mitochondria are dynamic organelles that undergo continual fission and fusion events that are regulated by large GTPases, such as DLP1 for fission and mitofusin 2 (MFN2) for fusion[1]. Unopposed mitochondrial fission or fusion causes human neurological diseases and is increasingly implicated in neurodegenerative diseases, including PD[2–4]. Proteins encoded by previously identified genes associated with familial PD—including α-synuclein (encoded by *SNCA*), PTEN-induced putative kinase (PINK) 1 (encoded by *PINK1*), the E3 ubiquitin ligase Parkin (encoded by *PARK2*), leucine-rich repeat kinase (LRRK) 2 (encoded by *LRRK2*) and the chaperone DJ-1 (encoded by *PARK7*)—are localized to mitochondria and are involved in the regulation of mitochondrial dynamics in the same or parallel pathways[5–12]. Therefore, an altered balance between mitochondrial fission and fusion is probably a common mechanism that leads to impaired mitochondrial quality control and the mitochondrial dysfunction that are critical to PD pathogenesis[13].

Recently, vacuolar protein sorting 35 (*VPS35*) was identified as the third gene associated with autosomal-dominant PD[14–16], after *SNCA* and *LRRK2*. The residue Asp620 is a mutational hotspot (with a common mutant being VPS35^{D620N}), whereas a rare, less-potent pathogenic variant is encoded by the *VPS35*^{R524W} allele[17,18]. As a key component of the retromer complex, VPS35 is important for endosome-to-Golgi and endosome–to–plasma membrane retrieval of membrane proteins[19,20]. Recent progress has extended the role of VPS35 in the formation of mitochondria-derived vesicles (MDVs)[21], which shuttle cargo from mitochondria to peroxisomes or lysosomes[22,23], suggesting that mitochondria may be a potential target site for VPS35 function. Therefore, we explored the potential involvement of VPS35 in the regulation of mitochondrial dynamics and function. During fission, DLP1 is recruited to the mitochondrial outer membrane and forms a large ring-like complex to promote fission[24]. Here we offer new insights into the cellular mechanism underlying the turnover of mitochondrial DLP1 complexes and the pathogenic mechanism of *VPS35* mutations in PD.

RESULTS

VPS35 mutations cause mitochondrial fragmentation *in vitro*

Rat primary cortical neurons that were transfected with mitoDsRed2 and constructs expressing human VPS35 variants were imaged for mitochondrial morphology. Neurons transfected with a vector control had mitochondria with a tubular morphology, with an average aspect ratio (major axis/minor axis) of 2.4 ± 0.2 (**Fig. 1a–c**). In contrast, neurons overexpressing wild-type *VPS35* (*VPS35*^{WT}) had mitochondria that were markedly decreased in length (**Supplementary Fig. 1a**), with an average aspect ratio of 1.87 ± 0.15 (**Fig. 1a–c**), suggesting that mitochondria were fragmented. We observed similarly fragmented

[1]Department of Pathology, Case Western Reserve University, Cleveland, Ohio, USA. [2]Electron Microscopy Core Facility, Case Western Reserve University, Cleveland, Ohio, USA. [3]Department of Pharmacology, Case Western Reserve University, Cleveland, Ohio, USA. [4]Center for Mitochondrial Diseases, Department of Medicine, Case Western Reserve University, Cleveland, Ohio, USA. [5]Institute of Clinical Neurosciences, Southmead Hospital, University of Bristol, Bristol, UK. [6]Trinity College Institute for Neuroscience, Trinity College Dublin, Dublin, Ireland. [7]The Henry Wellcome Integrated Signaling Laboratories, School of Biochemistry, University of Bristol, Bristol, UK. [8]Department of Neurology, Ruijin Hospital, Shanghai Jiao Tong University School of Medicine, Shanghai, China. [9]These authors contributed equally to this work. Correspondence should be addressed to X.Z. (xiongwei.zhu@case.edu), J.L. (jly0520@hotmail.com) or X.W. (xinglong.wang@case.edu).

Received 13 January; accepted 1 October; published online 30 November 2015; doi:10.1038/nm.3983

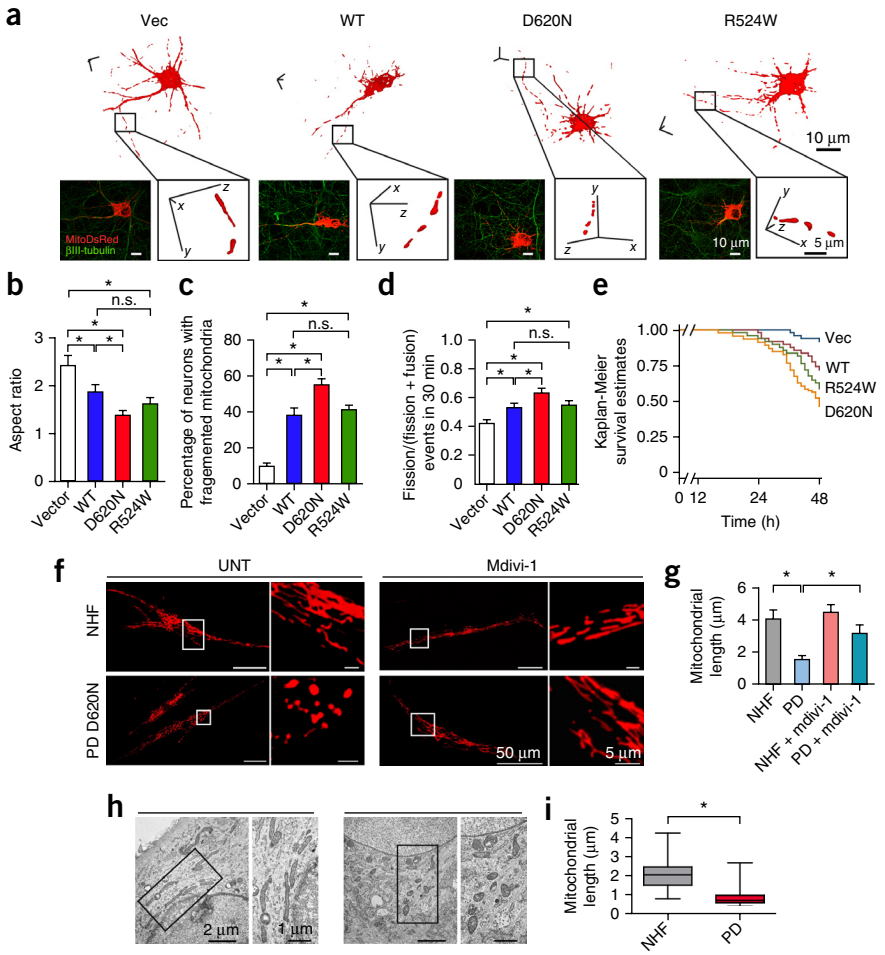


Figure 1 *VPS35* regulates mitochondrial dynamics *in vitro*. (**a**) Representative three-dimensional (3D) pictures (top) of mitochondria in rat cortical neurons cotransfected with either an empty-vector control plasmid (Vec) or plasmids expressing the indicated Flag-*VPS35* fusions and a construct encoding mitoDsRed2 (bottom left). A segment of axon (boxed area) was enlarged (bottom right). WT, $VPS35^{WT}$; D620N, $VPS35^{D620N}$; R524W, $VPS35^{R524W}$. Scale bars, 10 μm (microscopy images) and 5 μm (boxed area). (**b**,**c**) Quantification of mitochondrial aspect ratio (**b**) and percentage of neurons with fragmented mitochondria (**c**) in *VPS35*-overexpressing rat cortical neurons (vector-only control, $n = 35$; $VPS35^{WT}$, $n = 32$, $VPS35^{D620N}$, $n = 40$; $VPS35^{R524W}$, $n = 43$). (**d**) The ratio of fission and fission-plus-fusion events in live neurons expressing *VPS35* and mitoDsRed2 (vector-only control, $n = 43$; $VPS35^{WT}$, $n = 33$, $VPS35^{D620N}$, $n = 37$; $VPS35^{R524W}$, $n = 38$). (**e**) Measurement of neuronal viability in cortical neurons expressing *GFP*, *VPS35* and mitoDsRed2 (vector-only control, $n = 51$; $VPS35^{WT}$, $n = 46$, $VPS35^{D620N}$, $n = 55$; $VPS35^{R524W}$, $n = 51$). (**f**,**g**) Representative confocal images (**f**) and quantification of mitochondrial length (**g**) in PD D620N fibroblasts or in NHFs without (NHF, $n = 34$; $VPS35^{D620N}$ PD, $n = 44$) (**f**, left) or with (NHF + mdivi-1, $n = 27$; $VPS35^{D620N}$ PD + mdivi-1, $n = 53$) (**f**, right) mdivi-1 treatment. In **f**, enlarged images of the white boxed areas are shown to the right of each image. PD, PD D620N fibroblasts. Scale bars, 50 μm and 5 μm (enlarged images). (**h**,**i**) Representative EM micrographs of mitochondria (**h**) and quantification of mitochondrial length (**i**) in PD D620N fibroblasts (**h**, right) and NHFs (**h**, left). In **h**, enlarged images of the boxed areas are shown to the right. A total of 149 and 151 mitochondria from five randomly selected NHFs or PD D620N fibroblasts, respectively, were analyzed. Data are means ± s.e.m. from three independent experiments. $^*P < 0.05$; n.s., not significant; one-way analysis of variance (ANOVA) with Tukey's multiple-comparison test.

© 2015 Nature America, Inc. All rights reserved.

mitochondria in neurons overexpressing $VPS35^{R524W}$, whereas neurons overexpressing $VPS35^{D620N}$ had a more severe mitochondrial fragmentation phenotype. The neurite mitochondrial index, an index for mitochondrial density, was also significantly reduced in neurons overexpressing WT or mutant *VPS35* ($P < 0.05$; **Supplementary Fig. 1b**). We measured mitochondrial fission and fusion events by real-time imaging and found that the proportion of fission events (measured as the ratio of fission/(fission + fusion) events) was significantly increased in neurons overexpressing WT or mutated *VPS35*, as compared to neurons expressing the vector-only control ($P < 0.05$; **Fig. 1d**). Moreover, overexpression of $VPS35^{WT}$ or $VPS35^{R524W}$ caused significant neuronal loss, as compared to overexpression of the vector-only control, and this phenotype was more profound in $VPS35^{D620N}$-overexpressing cells ($P < 0.05$; **Fig. 1e**).

We further determined whether *Vps35* knockdown would induce an effect opposite to that of *VPS35* overexpression. We knocked down *Vps35* expression by using either of two different microRNA (miR)-based RNA interference (RNAi) constructs specific for *Vps35* and found that expression of either miR resulted in mitochondria with significantly increased lengths and aspect ratios and with a decreased proportion of fission events ($P < 0.05$; **Supplementary Fig. 1**). Of note, we also found that neurons treated with an RNAi construct that specifically suppresses expression of *Vps26*, which encodes another subunit of the retromer complex[25], showed a similar increase in the mitochondrial aspect ratio (**Supplementary Fig. 2a**,**b**). Knockdown of *Vps26* did not further increase the aspect ratio of mitochondria in cells in which *Vps35* had been knocked down. Notably, *VPS35* overexpression–induced mitochondrial fragmentation could be abolished by concurrent *Vps26* knockdown (**Supplementary Fig. 2c**,**d**), suggesting that *Vps35* and *Vps26* are involved in the same pathway.

Mitochondrial dynamics were also examined in M17 human dopaminergic neuroblastoma cells that stably overexpressed the mutated *VPS35* genes (**Supplementary Fig. 3**). Consistent with our observations in primary neurons, the mitochondrial aspect ratio decreased in M17 cells overexpressing $VPS35^{WT}$ or $VPS35^{R524W}$. This phenotype was exacerbated in $VPS35^{D620N}$-overexpressing M17 cells (**Supplementary Fig. 3**), whereas mitochondria became elongated in M17 cells in which *VPS35* expression was knocked down (**Supplementary Fig. 4**).

We further analyzed mitochondrial morphology in fibroblasts derived from an individual with PD who had the $VPS35^{D620N}$ mutation (hereafter referred to as PD D620N fibroblasts) and in normal human fibroblasts (NHFs) from age-matched control subjects (**Fig. 1f–i**). Confocal microscopy analysis revealed an interconnected mitochondrial network in NHFs, which was significantly fragmented in PD D620N fibroblasts (**Fig. 1f**,**g**). Electron microscopy (EM) analysis confirmed that mitochondria in the PD D620N fibroblasts were substantially more fragmented than those in the NHFs (**Fig. 1h**,**i**).

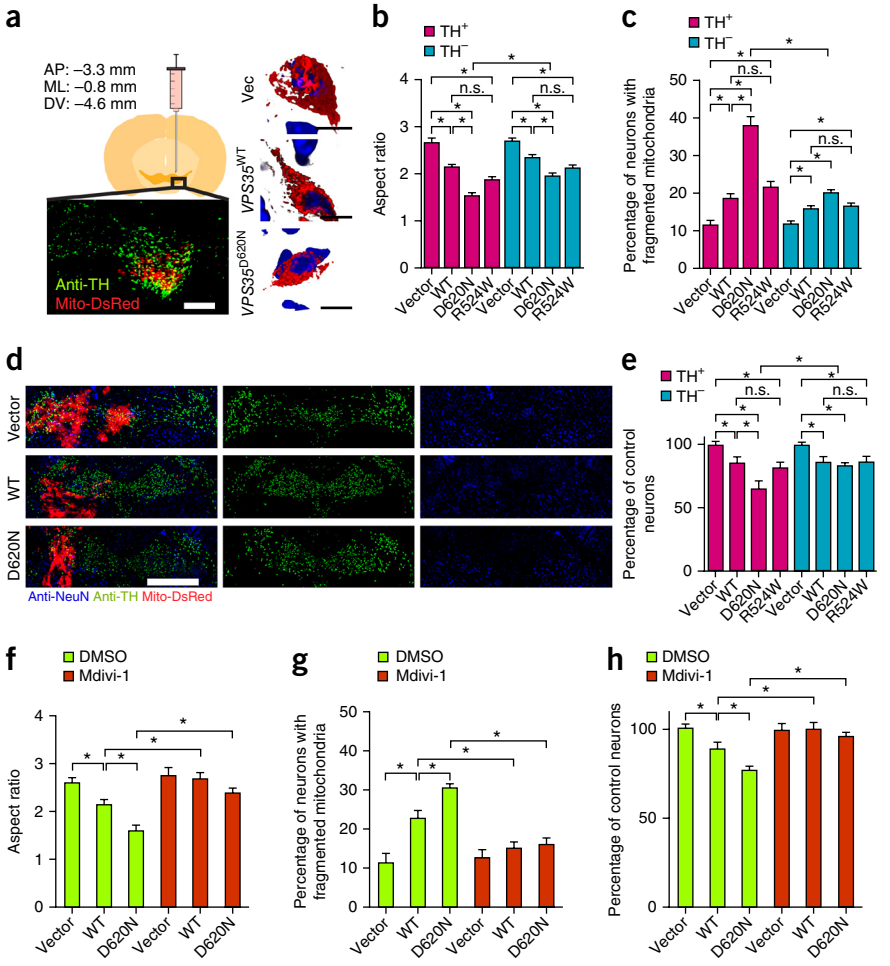


Figure 2 VPS35 regulates mitochondrial dynamics *in vivo*. (**a**) Left, schematic (top) and representative image (bottom) showing mitochondria (red) in positively transfected TH$^+$ neurons (green) after stereotactical injection of a lentivirus (that expresses *VPS35* and mitoDsRed2) unilaterally into the ventral tegmental area (VTA) of a mouse. Right, representative 3D images of mitochondria (red) in a TH$^+$ neuron in FVB mice injected with an empty-vector control (Vec) lentivirus (top) or a lentivirus that expresses *VPS35*^{WT} or VPS35^{D620N}. DAPI staining is shown in blue. AP, anteroposterior; ML, medial-lateral; DV, dorsal-ventral. Scale bars, 200 µm (left) and 5 µm (right). (**b**,**c**) Quantification of the mitochondrial aspect ratio (**b**) and the percentage of neurons with fragmented mitochondria (**c**) in TH$^+$ and TH$^-$ neurons in 2- to 3-month-old FVB mice injected with the indicated construct (TH$^+$ neurons: vector-only, $n = 20$; *VPS35*^{WT}, $n = 23$; *VPS35*^{D620N}, $n = 19$; *VPS35*^{R524W}, $n = 21$; TH$^-$ neurons: vector-only control, $n = 31$; *VPS35*^{WT}, $n = 36$; *VPS35*^{D620N}, $n = 35$; *VPS35*^{R524W}, $n = 31$; from three FVB mice per group). (**d**) Representative images of the substantia nigra in FVB mice ($n = 3$) injected with the indicated construct showing immunofluorescent costaining using antibodies specific for the neuronal protein NeuN (blue) and TH (green) and using mitoDsRed2. Scale bar, 400 µm. (**e**) Quantification of neuronal loss in TH$^+$ and TH$^-$ neurons in **c**. (**f**–**h**) Quantification of the mitochondrial aspect ratio (**f**), the percentage of neurons with fragmented mitochondria (**g**) and neuronal loss (**h**) in TH$^+$ neurons from FVB mice that were injected with lentiviruses expressing *VPS35* and treated with or without (DMSO) mdivi-1 (DMSO-treated: vector-only control, $n = 25$; *VPS35*^{WT}, $n = 26$; *VPS35*^{D620N}, $n = 27$; mdivi-1–treated: vector-only control, $n = 28$; *VPS35*^{WT}, $n = 22$; *VPS35*^{D620N}, $n = 24$; from three mice per group). Throughout, n represents number of neurons per group. Data are means ± s.e.m. $^*P < 0.05$; n.s., not significant; one-way ANOVA with Tukey's multiple-comparison test.

© 2015 Nature America, Inc. All rights reserved.

Treatment of the fibroblasts with the mitochondrial fission inhibitor mdivi-1 (ref. 26) restored mitochondrial length in the PD D620N fibroblasts (**Fig. 1f**,**g**), supporting the idea that the mitochondrial fragmentation phenotype observed in *VPS35*^{D620N}-overexpressing cells is because of increased mitochondrial fission.

VPS35 mutations lead to mitochondrial fragmentation *in vivo*

To determine the effect of the *VPS35* mutations *in vivo*, we stereotactically injected a lentivirus coexpressing mitoDsRed2 (to fluorescently label mitochondria) and WT or mutated human *VPS35* unilaterally into the substantia nigra of 2- to 3-month-old WT FVB or C57BL/6 mice (schematic in **Fig. 2a**) and imaged brain sections 3 weeks later. In mice of either background, neurons expressing *VPS35*^{WT} or *VPS35*^{R524W} had fragmented mitochondria, and the extent of mitochondrial fragmentation was more profound in neurons expressing the *VPS35*^{D620N} allele (**Fig. 2b**,**c** and **Supplementary Fig. 5a**,**b**). These phenotypes were distinct from the normal tubular-shaped mitochondria observed in the mouse neurons expressing the empty vector and mitoDsRed2. Massive degeneration of tyrosine hydroxylase–positive (TH$^+$) neurons occurs in the substantia nigra of brains from individuals with PD. There was a trend toward more severe mitochondrial fragmentation in the TH$^+$ neurons than in the TH$^-$ neurons in mice injected with the *VPS35*^{WT} or *VPS35*^{R524W} constructs, and this trend reached significance in mice injected with the *VPS35*^{D620N} construct ($P < 0.05$; **Fig. 2b**,**c**). Significant and comparable levels of neuronal loss, both in TH$^+$ and TH$^-$ neurons, were observed in the mice injected with the *VPS35*^{WT}- or *VPS35*^{R524W}-expressing construct (**Fig. 2d**,**e** and **Supplementary Fig. 5c**). The loss of TH$^+$ neurons correlated with enhanced mitochondrial fragmentation (data not shown) and was more profound in mice injected with the construct expressing *VPS35*^{D620N}. To determine the critical role of *VPS35*-induced mitochondrial fission *in vivo*, we treated the mice that had been injected with the *VPS35* constructs with mdivi-1. As expected, mdivi-1 treatment blocked *VPS35*-induced mitochondrial fragmentation in both TH$^+$ (**Fig. 2f**,**g**) and TH$^-$ neurons (data not shown) in the substantia nigra. Notably, mdivi-1 treatment also prevented *VPS35*-induced neuronal loss *in vivo* (**Fig. 2h**).

VPS35 mutations cause mitochondrial dysfunction

We assessed the effect of *VPS35* mutations on mitochondrial function, as well as on neuronal morphology and viability. As compared to M17 cells treated with the vector-only control, we observed substantial mitochondrial dysfunction in M17 cells that were overexpressing *VPS35*^{WT} or *VPS35*^{R524W}, and this phenotype was more severe in *VPS35*^{D620N}-overexpressing M17 cells, as evidenced by significantly increased production of reactive oxygen species

(ROS; data not shown), decreased ATP levels and decreased mitochondrial membrane potential (MMP) ($P < 0.05$, **Fig. 3a**,**b**). Measurement of oxygen consumption rates using the Seahorse XF24 analyzer[27,28] revealed impaired bioenergetics in these *VPS35*-expressing M17 cells, as evidenced by a significant reduction in the respiratory control ratio, the spare respiratory capacity and the coupling efficiency (**Supplementary Fig. 6**). Similar mitochondrial dysfunction (i.e., increased mitochondrial ROS and decreased MMP) to that induced by *VPS35* expression was also found in primary cortical neurons (data not shown). Of note, we also observed mitochondrial dysfunction and impaired bioenergetics in PD D620N fibroblasts, as compared to NHFs (**Fig. 3c**,**d** and **Supplementary Fig. 7**). Loss of dendritic spines and of synaptic boutons that stain positive for postsynaptic density protein (PSD) 95, a synaptic marker, was apparent in primary neurons expressing WT or mutated *VPS35* (**Fig. 3e**–**g**).

To determine whether excessive fission underlies the *VPS35*-induced mitochondrial and neuronal deficits, we inhibited mitochondrial fission either by overexpressing a dominant-negative mutant of DLP1 (encoded by $DLP1^{K38A}$) or by treating cells with mdivi-1 to block mitochondrial fragmentation (**Fig. 3h**–**j**). Mdivi-1 treatment did not

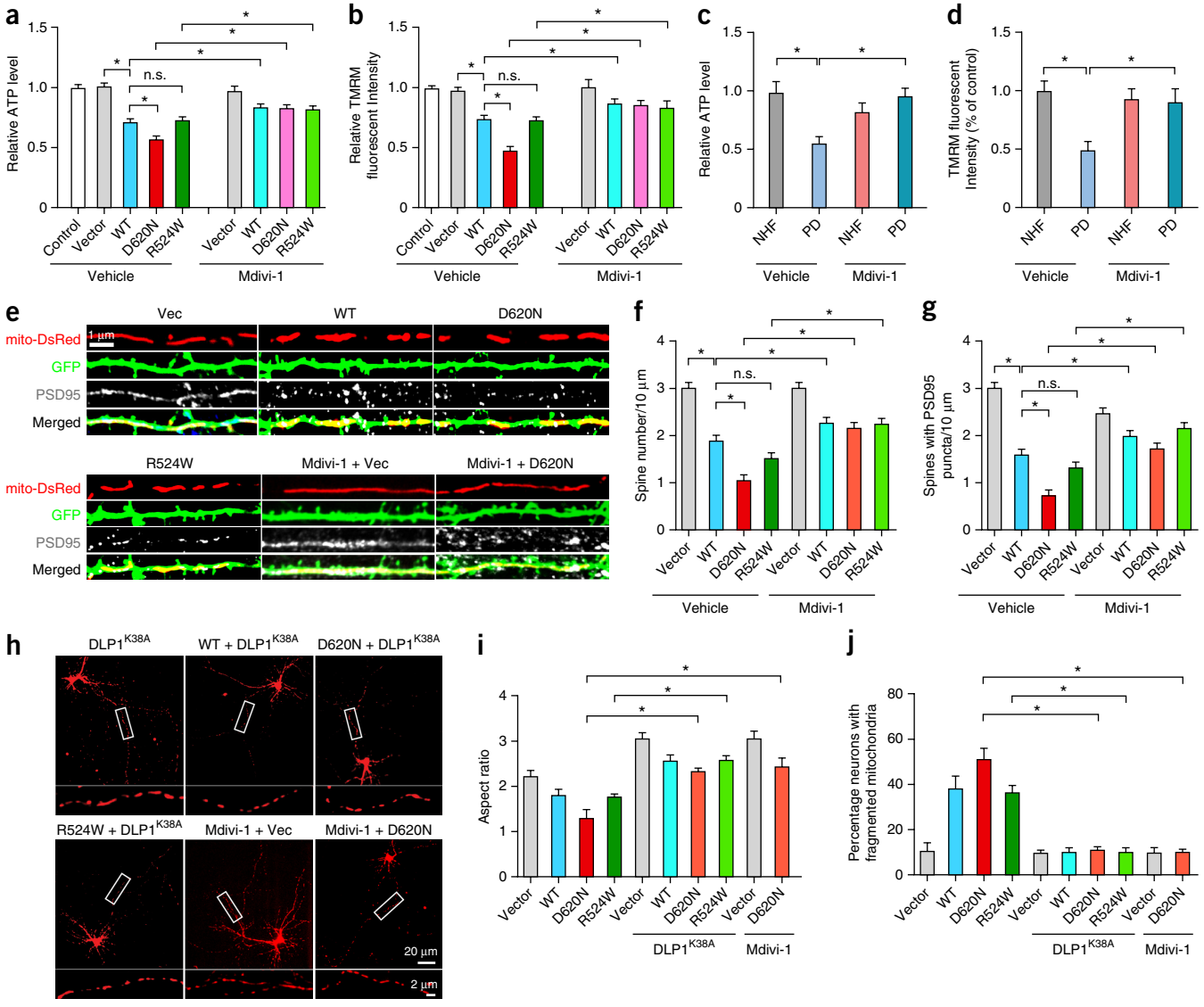


Figure 3 Inhibition of mitochondrial fission alleviates *VPS35*-induced mitochondrial dysfunction and neuronal deficits. (**a**–**d**) The intracellular levels of ATP (**a**,**c**) and mitochondrial membrane potential (MMP), as determined by a tetramethylrhodamine methyl ester (TMRM) fluorescent probe, (**b**,**d**) were measured in M17 cell lines stably expressing *VPS35* (**a**,**b**) and in NHFs and PD D620N fibroblasts (**c**,**d**) in the presence or absence of mdivi-1 treatment. (**e**–**g**) Representative images of dendrites (**e**) and quantification of dendritic spines (**f**) and PSD95$^+$ puncta (**g**) in primary rat cortical neurons (DIV14) cotransfected with mitoDsRed2 and the indicated *VPS35* construct, and treated with or without mdivi-1 (vehicle-treated: vector-only control, $n = 24$; $VPS35^{WT}$, $n = 23$; $VPS35^{D620N}$, $n = 25$; $VPS35^{R524W}$, $n = 28$; mdivi-1–treated: vector-only control, $n = 22$; $VPS35^{WT}$, $n = 27$; $VPS35^{D620N}$, $n = 25$; $VPS35^{R524W}$, $n = 25$). Scale bar, 1 µm. (**h**–**j**) Representative images of primary cortical neurons (boxed segment of axons are enlarged below) (**h**), and quantification of mitochondrial aspect ratio in the axon (**i**) and the percentage of neurons with fragmented mitochondria (**j**) in primary cortical neurons expressing mitoDsRed2, dominant-negative DLP1 (encoded by $DLP1^{K38A}$) and the indicated *VPS35* constructs (vector-only control, $n = 25$; $VPS35^{WT}$, $n = 23$; $VPS35^{D620N}$, $n = 26$; $VPS35^{R524W}$, $n = 28$; vector + $DLP1^{K38A}$, $n = 30$; $VPS35^{WT}$ + $DLP1^{K38A}$, $n = 21$; $VPS35^{D620N}$ + $DLP1^{K38A}$, $n = 22$; $VPS35^{R524W}$ + $DLP1^{K38A}$, $n = 29$; vector + mdivi-1, $n = 31$; $VPS35^{D620N}$ + mdivi-1, $n = 25$). Throughout, n represents the number of neurons per group. Data are means ± s.e.m. from three independent experiments. $^*P < 0.05$; n.s., not significant; one-way ANOVA with Tukey's multiple-comparison test.

© 2015 Nature America, Inc. All rights reserved.

affect DLP1 expression and phosphorylation (**Supplementary Fig. 8**). The inhibition of mitochondrial fragmentation rescued the *VPS35*-induced mitochondrial dysfunction both in neuronal cells overexpressing *VPS35* (**Fig. 3a**,**b**) and in PD D620N fibroblasts (**Fig. 3c**,**d** and **Supplementary Fig. 7**). Neuronal deficits (i.e., the loss of spines and PSD95 immunoreactivity) (**Fig. 3e**–**g**) were also rescued.

VPS35 regulates mitochondrial DLP1 complex turnover

Western blot analysis demonstrated that total DLP1 levels were slightly increased in *VPS35*-overexpressing M17 cells and decreased in M17 cells in which *VPS35* expression had been knocked down (**Supplementary Fig. 9**). Real-time PCR confirmed a substantial increase in *DLP1* mRNA levels in *VPS35*-overexpressing M17 cells (data not shown). We did not observe any significant changes for other fission and fusion proteins.

As compared with vector-only control lines, levels of mitochondrial DLP1 were significantly increased in *VPS35*^{WT}- or *VPS35*^{R524W}-overexpressing M17 cells, and this became more profound in *VPS35*^{D620N}-overexpressing M17 cells but significantly reduced in M17 cells in which *VPS35* expression had been knocked down ($P < 0.05$, **Fig. 4a**,**b**), suggesting that VPS35 facilitates mitochondrial translocation of DLP1 and that this is enhanced by PD-associated mutations. To corroborate this finding, we imaged mitochondrial DLP1 in M17 cells that were fixed and immunostained for DLP1. Unexpectedly, the density and average size of the mitochondrial DLP1 puncta were significantly decreased in *VPS35*-overexpressing M17 cells but significantly increased in M17 cells knocked down for *VPS35* ($P < 0.05$, **Fig. 4c**,**d**). Because mitochondrial DLP1 assembles into large complexes and as the DLP1 puncta on mitochondria probably represent the mitochondrial DLP1 complex[29], this finding suggests that VPS35 may regulate

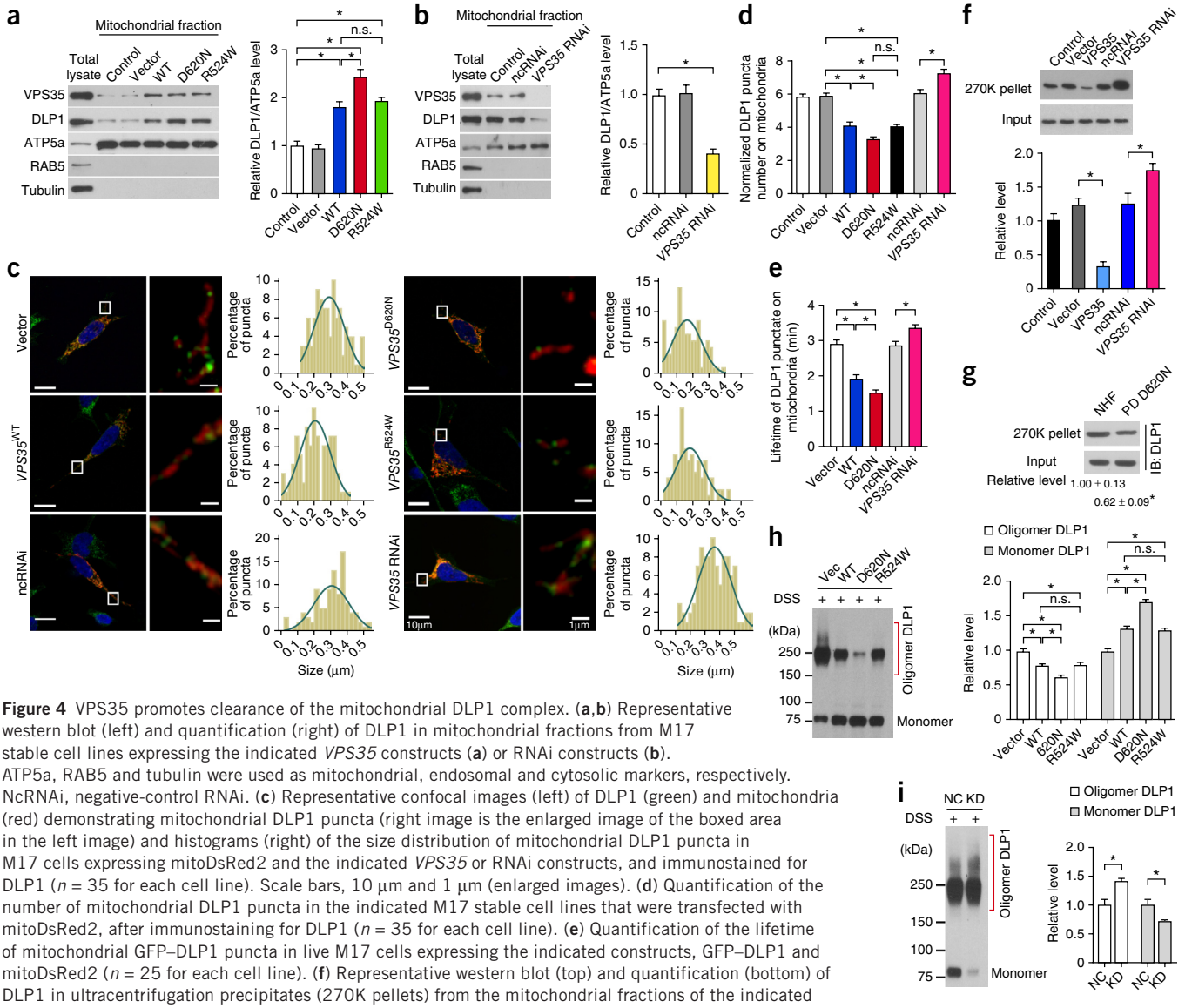


Figure 4 VPS35 promotes clearance of the mitochondrial DLP1 complex. (**a**,**b**) Representative western blot (left) and quantification (right) of DLP1 in mitochondrial fractions from M17 stable cell lines expressing the indicated *VPS35* constructs (**a**) or RNAi constructs (**b**). ATP5a, RAB5 and tubulin were used as mitochondrial, endosomal and cytosolic markers, respectively. NcRNAi, negative-control RNAi. (**c**) Representative confocal images (left) of DLP1 (green) and mitochondria (red) demonstrating mitochondrial DLP1 puncta (right image is the enlarged image of the boxed area in the left image) and histograms (right) of the size distribution of mitochondrial DLP1 puncta in M17 cells expressing mitoDsRed2 and the indicated *VPS35* or RNAi constructs, and immunostained for DLP1 ($n = 35$ for each cell line). Scale bars, 10 μm and 1 μm (enlarged images). (**d**) Quantification of the number of mitochondrial DLP1 puncta in the indicated M17 stable cell lines that were transfected with mitoDsRed2, after immunostaining for DLP1 ($n = 35$ for each cell line). (**e**) Quantification of the lifetime of mitochondrial GFP–DLP1 puncta in live M17 cells expressing the indicated constructs, GFP–DLP1 and mitoDsRed2 ($n = 25$ for each cell line). (**f**) Representative western blot (top) and quantification (bottom) of DLP1 in ultracentrifugation precipitates (270K pellets) from the mitochondrial fractions of the indicated M17 stable cell lines, after treatment with DTME. (**g**) Representative western blot and quantification of DLP1 (denoted below the blot) in the 270K pellets from mitochondrial fractions of PD D620N fibroblasts or NHFs, after treatment with DTME. (**h**,**i**) Representative western blot of DLP1 (left) and quantification (right) of oligomeric and monomeric DLP1 in the mitochondrial fraction of *VPS35*-expressing M17 cells (**h**) or M17 cells in which *VPS35* was knocked down (**i**), after treatment with DSS. NC, negative control; KD, *VPS35* knockdown. Throughout, *n* represents number of neurons per group. Data are means ± s.e.m. from three independent experiments from three stable M17 clonal lines. $^*P < 0.05$; n.s., not significant; one-way ANOVA with Tukey's multiple-comparison test.

© 2015 Nature America, Inc. All rights reserved.

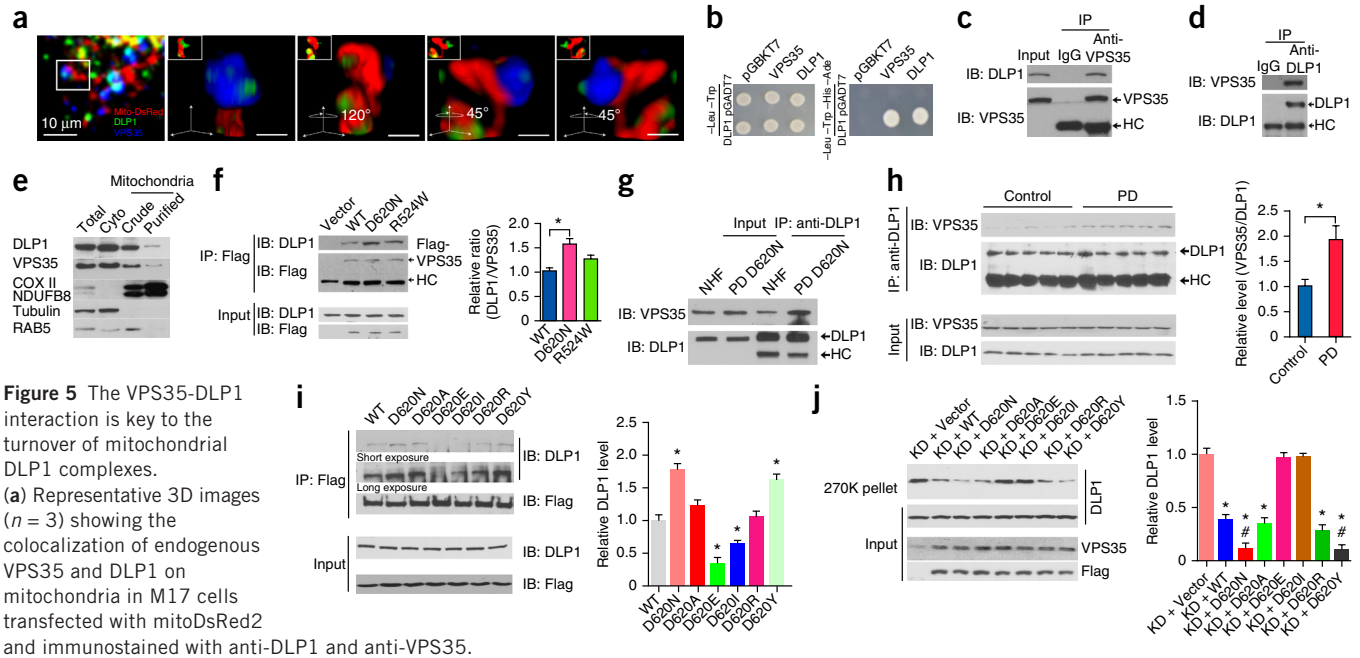


Figure 5 The VPS35-DLP1 interaction is key to the turnover of mitochondrial DLP1 complexes.
(**a**) Representative 3D images ($n = 3$) showing the colocalization of endogenous VPS35 and DLP1 on mitochondria in M17 cells transfected with mitoDsRed2 and immunostained with anti-DLP1 and anti-VPS35. Boxed area in the left image was enlarged and viewed at different angles. Scale bars, 10 µm (left image) and 2 µm (enlarged images). (**b**) Yeast two-hybrid analysis of VPS35-DLP1 interaction. All positively cotransformed cells grew on SD plates lacking leucine and tryptophan (left). After being streaked onto high-stringency plates (SD plates lacking leucine, tryptophan, histidine and adenine), only clones cotransformed with pGBKT7-DLP1 and pGADT7-DLP1 (positive control) or pGBKT7-VPS35 and pGADT7-DLP1 could grow (right) ($n = 3$). pGBKT7 and pGADT7 are the empty vectors. (**c**,**d**) Representative western blot analyses ($n = 3$) for the presence of DLP1 and VPS35 in VPS35 immunoprecipitates (**c**) or DLP1 immunoprecipitates (**d**) from normal M17 cells. HC, heavy chain; IgG, isotype control antibody. (**e**) Representative western blot analysis ($n = 3$) for the presence of endogenous DLP1 and VPS35 in mitochondrial fractions from M17 cells. COX II and NDUFB8 (NADH dehydrogenase (ubiquinone) 1 beta subcomplex, 8) were used as mitochondrial markers; tubulin and RAB5 were used as cytosolic and endosomal markers, respectively. (**f**) Representative western blot (left; $n = 3$) and quantification (right) of DLP1 in Flag immunoprecipitates of the highly purified mitochondrial fraction prepared from M17 cells expressing Flag-tagged VPS35 variants. (**g**) Representative western blot ($n = 3$) of VPS35 and DLP1 in DLP1 immunoprecipitates from PD D620N fibroblasts and NHFs. (**h**) Representative western blot analysis (left) and quantification (right) of VPS35 in DLP1 immunoprecipitates from homogenates of the midbrains of individuals with sporadic PD and age-matched controls ($n = 5$ per group). (**i**) Representative western blot analysis (left) and quantification (right; $n = 3$) of DLP1 in Flag immunoprecipitate from M17 cells expressing the indicated Flag-tagged VPS35 mutants. D620A, *VPS35*^{D620A}; D620E; *VPS35*^{D620E}; D620I, *VPS35*^{D620I}; D620R; *VPS35*^{D620R}; D620Y; *VPS35*^{D620Y}. (**j**) Representative western blot analysis (left) and quantification (right; $n = 3$) of DLP1 in the 270K pellets from mitochondrial fractions of M17 cell lines knocked down for endogenous VPS35 and expressing the indicated Flag-tagged VPS35 mutants. Throughout, data are means ± s.e.m. from three independent experiments. $^*P < 0.05$, as compared with KD + Vector; $\#P < 0.05$ as compared with KD + WT; one-way ANOVA with Tukey's multiple-comparison test (except for **h**, which used Student's *t*-test).

© 2015 Nature America, Inc. All rights reserved.

the clearance of mitochondrial DLP1 complexes and facilitate the recruitment of fission-competent forms of DLP1.

To test this possibility, we expressed GFP-tagged DLP1 (GFP–DLP1) in M17 cells and used the 'fluorescent recovery after photobleaching' (FRAP) technique to measure the lifetime of mitochondrial GFP–DLP1 puncta by real-time imaging. *VPS35* overexpression significantly shortened, whereas *VPS35* knockdown significantly extended, the lifetime of the puncta ($P < 0.05$; **Fig. 4e**). This is probably not because of the difference in diffusion-limited kinetics, as the fluorescence recovery of mitochondrial GFP–DLP1 was not dependent on the size of the bleached area and because all of the stable cell lines had similar kinetics of GFP–DLP1 recovery in cytosolic areas that were devoid of mitochondria (data not shown). To determine the levels of mitochondrial DLP1 complexes, we prepared mitochondrial fractions from cells that were exposed to the reversible crosslinking agent dithiobismaleimidoethane (DTME), precipitated large mitochondrial protein complexes from these fractions by ultracentrifugation (which we refer to as 270K pellets) and analyzed DLP1 levels using SDS-PAGE and western blotting. DLP1 levels were significantly decreased in the 270K pellets from *VPS35*^{WT}-overexpressing M17 cells but significantly increased in pellets from M17 cells after knocking down *VPS35* expression (**Fig. 4f**). Notably, DLP1 levels were also significantly decreased in 270K pellets from PD D620N fibroblasts, as compared to DLP1 levels in 270K pellets from NHFs ($P < 0.05$; **Fig. 4g**). The use of an irreversible cross-linking agent (such as disuccinimidyl suberate (DSS)) allows direct detection of oligomeric DLP1 complexes and monomeric DLP1 (refs. 29–32). Indeed, western blot analyses of mitochondrial fractions from DSS-treated cells demonstrated that levels of oligomeric DLP1 complexes were significantly decreased in *VPS35*-overexpressing cells but significantly increased in M17 cells after knocking down *VPS35* expression (**Fig. 4h**,**i**). In contrast, levels of monomeric mitochondrial DLP1 was significantly increased in cells in which *VPS35* was overexpressed but decreased in cells in which *VPS35* expression was knocked down (**Fig. 4h**,**i**). Knockdown of *VPS26* expression increased the number of mitochondrial DLP1 puncta and the levels of oligomeric DLP1complexes, but did not cause any further increases in these phenotypes in cells that had also been knocked down for *VPS35* expression (**Supplementary Fig. 10a**,**b**). Of note, the effect of *VPS35* overexpression on mitochondrial DLP1 complexes could be reversed by *VPS26* knockdown (**Supplementary Fig. 10c**).

VPS35-DLP1 interaction is key to the turnover of mitochondrial DLP1

To determine the biochemical basis of the regulatory role of VPS35 in mitochondrial dynamics, we investigated whether VPS35

interacts with DLP1. We imaged M17 cells that were transfected with mitoDsRed2 and immunostained with antibodies specific for DLP1 or VPS35. The 3D-reconstructed images demonstrated the colocalization of DLP1 puncta and VPS35 on mitochondria (**Fig. 5a**). We also found a strong interaction between VPS35 and DLP1 using yeast two-hybrid analysis (**Fig. 5b**). In M17 cells, endogenous VPS35 could be co-immunoprecipitated by the DLP1-specific antibody and vice versa (**Fig. 5c**,**d**). We confirmed the presence of endogenous VPS35 in purified mitochondrial fractions (**Fig. 5e**)[21]. Indeed, endogenous DLP1 in mitochondrial fractions co-immunoprecipitated with VPS35 (**Fig. 5f**). By using purified mitochondrial fractions and a VPS35-specific antibody, we found that significantly more DLP1 was pulled down from M17 cells expressing VPS35^{D620N} than from cells expressing VPS35^{WT}, suggesting that there was an enhanced interaction between DLP1 and the VPS35^{D620N} mutant (**Fig. 5f**). Indeed, increased VPS35-DLP1 interaction was confirmed in the PD D620N fibroblasts as compared

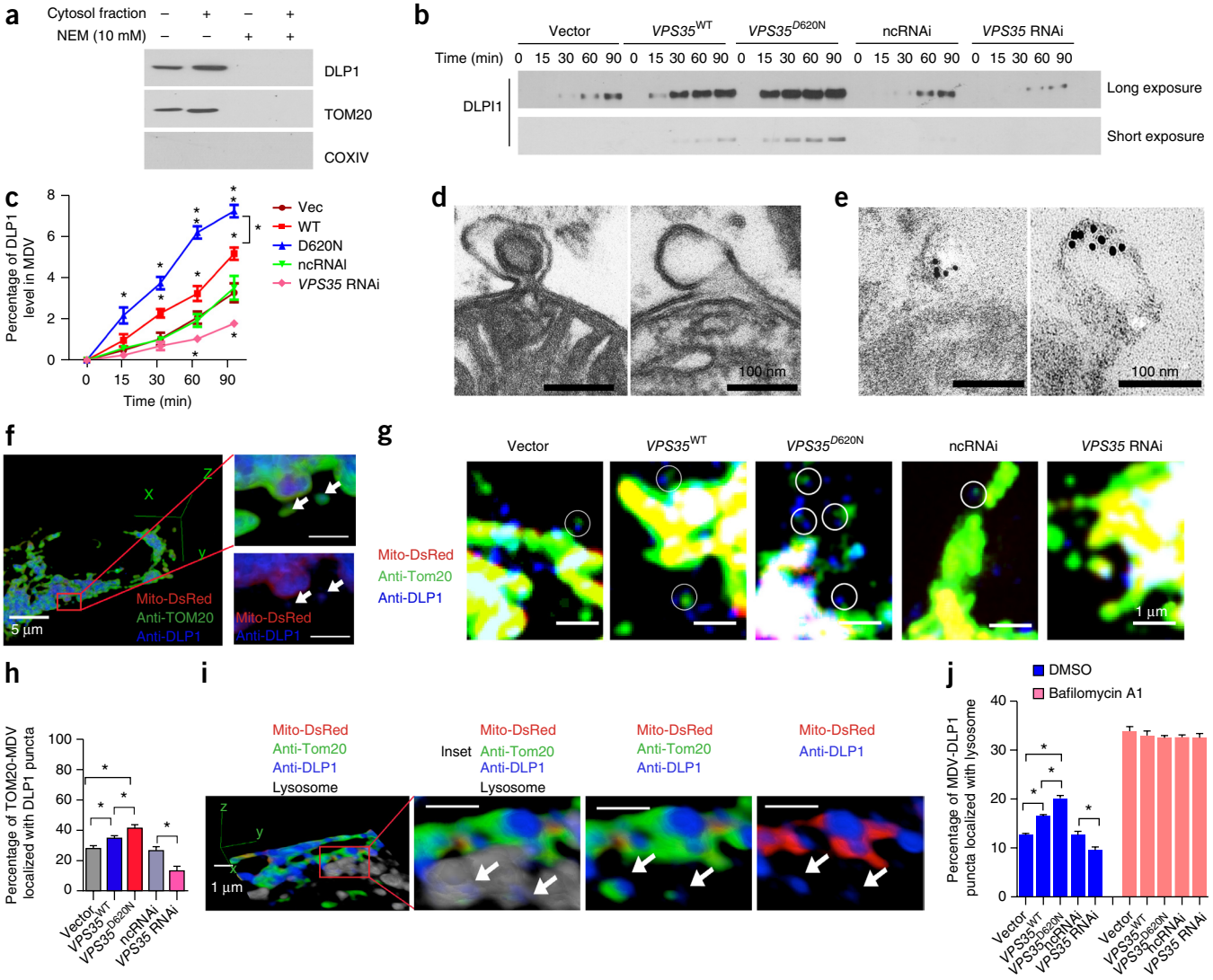


Figure 6 The VPS35-containing retromer mediates mitochondrial DLP1 complex degradation through an MDV-to-lysosome pathway. (**a**) Representative western blot analysis ($n = 3$) for the presence of DLP1 in *in vitro*–reconstituted MDVs. TOM20 and COX IV were used as positive and negative controls for MDVs, respectively. (**b**,**c**) Representative western blot analysis ($n = 3$) (**b**) and quantification (**c**) of DLP1 in the *in vitro*–reconstituted MDVs in the presence of cytosolic fractions from the indicated M17 cells. (**d**) Representative electron micrographs ($n = 7$) of purified mitochondria highlighting double-membraned (left) and single-membraned (right) MDVs still attached to the mitochondrion. Scale bars, 100 nm. (**e**) Representative immuno-EM micrographs ($n = 5$) showing the specific labeling of DLP1-immunoreactive gold particles associated with MDVs. Scale bars, 100 nm. (**f**) Representative images ($n = 3$) showing the colocalization of DLP1 puncta and MDVs (TOM20^{+}mitoDsRed2^{-}) (arrows) in M17 cells. Scale bars, 5 µm and 1 µm (enlarged images). (**g**,**h**) Representative confocal images (**g**) and quantification (**h**) of the colocalization of DLP1 puncta and MDVs (as highlighted in circles) in the indicated M17 stable cell lines. (vector-only control, $n = 31$; *VPS35*^{WT}, $n = 35$; *VPS35*^{D620N}, $n = 37$; negative control (nc) RNAi, $n = 28$; *VPS35* RNAi, $n = 31$). Scale bars, 1 µm. (**i**) Representative 3D-reconstructed images ($n = 3$) of an M17 cell (left) showing the colocalization of DLP1 puncta and MDVs in the lysosome (left, boxed area). Enlarged views of the boxed area are shown to the right. Arrows point to MDVs-associated DLP1 puncta in a lysosome. Scale bars, 1 µm (left) and 1 µm (enlarged images). (**j**) Quantification of the percentage of MDVs associated with DLP1 puncta within lysosomes with or without bafilomycin A1 treatment (DMSO-treated: vector-only control, $n = 33$; *VPS35*^{WT}, $n = 28$; *VPS35*^{D620N}, $n = 35$; ncRNAi, $n = 37$; *VPS35* RNAi, $n = 31$; bafilomycin A1–treated: vector-only control, $n = 31$; *VPS35*^{WT}, $n = 35$; *VPS35*^{D620N}, $n = 36$; ncRNAi, $n = 27$; *VPS35* RNAi, $n = 31$). Data are means ± s.e.m. from three independent experiments. $^{*}P < 0.05$; one-way ANOVA with Tukey's multiple-comparison test.

© 2015 Nature America, Inc. All rights reserved.

to that in NHFs (**Fig. 5g**). Increased VPS35-DLP1 interaction was also found in hydrogen peroxide–treated or paraquat-treated M17 cells, which was inhibited by concurrent treatment with the antioxidant *N*-acetylcysteine (**Supplementary Fig. 11**), suggesting that oxidative modification may enhance the VPS35-DLP1 interaction. Increased oxidative stress is a prominent feature of PD[2], and increased VPS35-DLP1 interactions were found in postmortem brain samples of individuals with sporadic PD (**Fig. 5h**).

The VPS35^{D620N} mutant showed an enhanced interaction with DLP1 (**Fig. 5f**,**g**). Not unexpectedly, mutations introduced at residue D620 differentially impacted the VPS35-DLP1 interaction—VPS35^{D620E} and VPS35^{D620I} decreased the interaction, VPS35^{D620A} and VPS35^{D620R} did not affect it, and VPS35^{D620Y} increased VPS35's interaction with DLP1 (**Fig. 5i**). These mutants also had differential effects on the accumulation of mitochondrial DLP1 complexes in M17 cells after knockdown of endogenous *VPS35* (**Fig. 5j**). Overexpression of VPS35^{WT}, VPS35^{D620A} or VPS35^{D620R} significantly reduced the levels of mitochondrial DLP1 complexes in the 270K pellets, whereas overexpression of VPS35^{D620N} or VPS35^{D620Y} caused even further reductions ($P < 0.05$). Overexpression of VPS35^{D620E} or VPS35^{D620I} did not have any effect on the levels of mitochondrial DLP1 complexes (**Fig. 5j**). Consistently, these mutants also had differential effects on the elongated mitochondrial morphology observed in M17 cells after *VPS35* knockdown (**Supplementary Fig. 12a**,**b**). Overexpression of VPS35^{WT}, VPS35^{D620A} or VPS35^{D620R} enhanced fission to restore the normal filamentous mitochondrial morphology. Overexpression of VPS35^{D620N} or VPS35^{D620Y} resulted in even shorter mitochondria, whereas expression of VPS35^{D620E} or VPS35^{D620I} failed to rescue the elongated mitochondrial morphology (**Supplementary Fig. 12a**,**b**), suggesting that fission is deficient in cells expressing the latter two mutants. In a control experiment, we found that knocking down *VPS35* reduced retromer activity, as evidenced by reduced recycling of the fatty-acid translocator (FAT; also referred to as CD36)(ref. 33), and that expression of each VPS35 mutant (under these conditions) restored FAT (CD36) recycling to a level comparable to that observed with endogenous VPS35 (**Supplementary Fig. 12c**), demonstrating that retromer function was not impaired in these mutants. Collectively, these data strongly support that the VPS35-DLP1 interaction is essential for mitochondrial DLP1 complex turnover, which is required for efficient mitochondrial fission.

MDV mediates VPS35-dependent mitochondrial DLP1 turnover

The retromer is involved in MDV formation, and MDVs can transport mitochondrial proteins to lysosomes[22,34]. We investigated whether DLP1 is localized to MDVs. MDVs contain mitochondrial outer-membrane proteins, such as TOM20, but not mitochondrial matrix proteins such as cytochrome c oxidase (COX) IV and mitoDsRed2 (ref. 21). To reconstitute MDVs *in vitro*, we used a cell-free budding assay[35]. Western blot analysis demonstrated the presence of trypsin-resistant proteins incorporated within MDVs, such as TOM20, and the absence of COX IV in the post-mitochondria supernatant after treatment with trypsin (**Fig. 6a**), confirming the successful reconstitution of MDVs *in vitro*. As expected, the TOM20 signal in reconstituted MDVs was enhanced by addition of a cytosolic fraction to the *in vitro* reaction mixture and abolished in the presence of *N*-ethymaleimide (NEM), a cell-free membrane transport inhibitor (**Fig. 6a**). DLP1 behaved similarly to TOM20 (**Fig. 6a**), suggesting that DLP1 is a cargo of MDVs. The enrichment of trypsin-resistant DLP1 incorporated within MDVs in the post-mitochondrial supernatant after treatment with trypsin was time dependent (i.e., the longer the treatment, the more the accumulation of DLP1). Moreover, DLP1 enrichment was significantly stimulated by the presence of cytosolic fractions from *VPS35*-overexpressing versus vector-only control M17 cells ($P < 0.05$; **Fig. 6b**,**c**) and significantly reduced in the presence of cytosolic fractions from M17 cells after knocking down *VPS35* expression ($P < 0.05$; **Fig. 6b**,**c**).

By using electron microscopy (EM) on purified mitochondria, we readily observed 60- to 100-nm, single- or double-membraned vesicular structures attached to the mitochondrion, consistent with previous descriptions of MDVs[36] (**Fig. 6d**). Immuno-EM with a highly specific antibody to DLP1 (**Supplementary Fig. 13**) revealed the presence of DLP1^{+} immunogold particles in these MDVs (**Fig. 6e**). This was corroborated by confocal imaging analyses in which DLP1 puncta colocalized with TOM20^{+}mitoDsRed2^{-} MDVs in M17 cells (**Fig. 6f**). Of note, the colocalization of DLP1 with MDVs was significantly increased in M17 cells after *VPS35* overexpression but decreased in M17 cells after *VPS35* knockdown (**Fig. 6g**,**h**), suggesting that VPS35 mediates the MDV-dependent transport of DLP1.

3D-reconstructed images showed the presence of DLP1 puncta–associated MDVs in lysosomes (**Fig. 6i**), which was reduced by *VPS35* knockdown but increased by overexpression of *VPS35*^{WT} or *VPS35*^{D620N} (**Fig. 6j**). The presence of DLP1 puncta–associated MDVs in lysosomes was inversely correlated with the density of the mitochondrial DLP1 puncta (data not shown). Indeed, inhibition of lysosomal degradation by treating cells with bafilomycin A1 led to increased accumulation of DLP1 puncta–associated MDVs in lysosomes (**Fig. 6j**), thus confirming degradation to be the final fate of the DLP1 complexes that are trafficked to lysosomes via MDVs. We found no differences in peroxisomal DLP1 levels in cells that overexpressed *VPS35* or those in which *VPS35* was knocked down (**Supplementary Fig. 14**), suggesting that VPS35-dependent DLP1-containing MDVs do not traffic to peroxisomes.

DISCUSSION

We found that the PD-associated *VPS35*^{D620N} mutation causes extensive mitochondrial fragmentation and functional deficits, and leads to neuronal loss both *in vitro* and in the substantia nigra of mouse brain *in vivo*. This could be rescued by inhibiting excessive mitochondrial fission, suggesting that the *VPS35* mutation probably causes neurodegeneration through damaging effects on mitochondrial dynamics and function. These effects of the PD-associated *VPS35* mutation are probably specific effects of the mutation and independent of potential overexpression artifacts because: (i) in the *VPS35*^{D620N}-expressing fibroblasts from an individual with PD, mitochondria were fragmented and functionally impaired; (ii) elongated mitochondria that were observed in M17 cells after *VPS35* knockdown could be restored to their normal filamentous shape by re-expression of *VPS35*^{WT}; however, the elongated mitochondria were fragmented by expression of *VPS35*^{D620N} at levels similar to those of *VPS35*^{WT}; and (iii) a VPS35-DLP1 interaction was found in normal M17 cells and in NHFs, and this interaction was found to be enhanced in fibroblasts from an individual with PD who has the *VPS35*^{D620N} allele.

Mechanistically, we describe a novel concept for the biology of mitochondrial fission by revealing the involvement of VPS35 and the retromer complex in the recycling of mitochondrial DLP1 complexes and in the regulation of mitochondrial fission (**Supplementary Fig. 15**). DLP1 complexes present on the mitochondrial outer membrane remain with the daughter mitochondrion after fission[37] and probably become inhibitory for subsequent fission events owing to the occupancy of fission sites or to the sequestration of DLP1 recruiting

© 2015 Nature America, Inc. All rights reserved.

factors[29–32,38,39]. Here we demonstrated that the retromer, through a VPS35-DLP1 interaction, mediates the removal of these DLP1 complexes from mitochondria and transports them, via the formation and trafficking of MDVs, to lysosomes for degradation—a process that effectively alleviates the inhibitory effects of the mitochondrial DLP1 complexes and that is probably required for efficient mitochondrial fission. The PD-associated VPS35 mutant resulted in an increased VPS35-DLP1 interaction and enhanced the retromer-dependent turnover of mitochondrial DLP1 complexes via MDV-mediated trafficking. Thus, it tipped the balance of mitochondrial dynamics toward excessive fission, which has been found to lead to mitochondrial dysfunction and neuronal loss[40]. We further demonstrated that increased oxidative stress enhances the VPS35-DLP1 interaction, a mechanism that may underlie the increased VPS35-DLP1 interaction observed in the brains of individuals with sporadic PD. These data support a more general role for the dysregulation of VPS35-mediated mitochondrial DLP1 complex turnover in causing abnormal mitochondrial dynamics and mitochondrial dysfunction that are critical to PD pathogenesis.

Various PD-associated proteins are involved in the regulation of mitochondrial dynamics. PINK1 and Parkin regulate the ubiquitination and degradation of MFN2 and DLP1, whereas LRRK2 increases DLP1 recruitment to mitochondria[5,8,9]. Here we revealed a novel cellular mechanism for the regulation of mitochondrial fission at the level of turnover of the mitochondrial DLP1 complex; this was enhanced by the PD-associated VPS35^{D620N} mutant. Nevertheless, our study does not exclude the possibility that other cellular functions may be negatively impacted by *VPS35* mutations. Recent studies have revealed that the *VPS35*^{D620N} mutation also leads to a defect in its binding to the Wiskott-Aldrich syndrome protein and scar homolog (WASH) complex and perturbation in endosome-to-Golgi transport and autophagosome biogenesis[41–43].

METHODS

Methods and any associated references are available in the online version of the paper.

Note: Any Supplementary Information and Source Data files are available in the online version of the paper.

ACKNOWLEDGMENTS

This work is partly supported by the US National Institutes of Health (NIH) (grant no. NS071184 (X.Z.), NS083498 (X.Z.) and NS085747 (X.W.)); the Clinical and Translational Science Collaborative of Cleveland; the National Center for Advancing Translational Sciences component of the NIH and the NIH Roadmap for Medical Research (grant no. UL1TR000439; pilot award to X.Z.); the Chinese Overseas, Hong Kong and Macao Scholars Collaborated Research Fund (grant no. 81228007; X.Z.); the Shanghai Orientalist program (X.Z.), the Dr. Robert M. Kohrman Memorial Fund (X.Z.); the National Natural Science Fund of China (grant no. 81071024, 81171202, 30870879, 81228007 and 81471287; all to J.L.); the Wellcome Trust (grant no. 089928 and 085743; both to P.J.C.) and the Medical Research Council (grant no. MR/K018299/1; P.J.C.). We thank I. Kelmanson (Evrogen) for the mito-TagBFP construct and Y. Yoon (University of Rochester) for the *DLP1*^{WT} and *DLP1*^{K38A} constructs. Some Parkinson's disease tissue samples were obtained from the Harvard Brain Tissue Resource Center, which is supported in part by the Public Health Service contract (HHS-NIH-NIDA (MH)-13-265), and from the NIH Neurobiobank at the University of Maryland.

AUTHOR CONTRIBUTIONS

X.Z. and X.W. conceived and directed the project, interpreted the results and wrote the manuscript. W.W. and X.W. designed and carried out experiments, analyzed results and generated figures. H.F. helped with electron microscopy (EM) and the immuno-EM study; C.H. helped with bioenergetics measurements; A.L.W., M.A.C. and P.J.C. contributed fibroblasts from the individual with PD who has the *VPS35*^{D620N} mutation and provided feedback on the manuscript; and J.L. contributed to the conception of the project, design of the experiments and the interpretation of results, and provided feedback on the manuscript.

COMPETING FINANCIAL INTERESTS

The authors declare no competing financial interests.

Reprints and permissions information is available online at http://www.nature.com/reprints/index.html.

1. Chan, D.C. Fusion and fission: interlinked processes critical for mitochondrial health. *Annu. Rev. Genet.* **46**, 265–287 (2012).
2. Yan, M.H., Wang, X. & Zhu, X. Mitochondrial defects and oxidative stress in Alzheimer disease and Parkinson disease. *Free Radic. Biol. Med.* **62**, 90–101 (2013).
3. Burté, F., Carelli, V., Chinnery, P.F. & Yu-Wai-Man,, P. Disturbed mitochondrial dynamics and neurodegenerative disorders. *Nat. Rev. Neurol.* **11**, 11–24 (2015).
4. Wang, X. *et al.* Amyloid-β overproduction causes abnormal mitochondrial dynamics via differential modulation of mitochondrial fission/fusion proteins. *Proc. Natl. Acad. Sci. USA* **105**, 19318–19323 (2008).
5. Chen, Y. & Dorn, G.W. PINK1-phosphorylated mitofusin 2 is a parkin receptor for culling damaged mitochondria. *Science* **340**, 471–475 (2013).
6. Clark, I.E. *et al. Drosophila* Pink1 is required for mitochondrial function and interacts genetically with parkin. *Nature* **441**, 1162–1166 (2006).
7. Narendra, D., Tanaka, A., Suen, D.F. & Youle, R.J. Parkin is recruited selectively to impaired mitochondria and promotes their autophagy. *J. Cell Biol.* **183**, 795–803 (2008).
8. Wang, X. *et al.* LRRK2 regulates mitochondrial dynamics and function through direct interaction with DLP1. *Hum. Mol. Genet.* **21**, 1931–1944 (2012).
9. Su, Y.C. & Qi, X. Inhibition of excessive mitochondrial fission reduced aberrant autophagy and neuronal damage caused by the *LRRK2*^{G2019S} mutation. *Hum. Mol. Genet.* **22**, 4545–4561 (2013).
10. Irrcher, I. *et al.* Loss of the Parkinson's disease–linked gene *DJ-1* perturbs mitochondrial dynamics. *Hum. Mol. Genet.* **19**, 3734–3746 (2010).
11. Wang, X. *et al.* Parkinson's disease–associated *DJ-1* mutations impair mitochondrial dynamics and cause mitochondrial dysfunction. *J. Neurochem.* **121**, 830–839 (2012).
12. Lim, K.L., Ng, X.H., Grace, L.G. & Yao, T.P. Mitochondrial dynamics and Parkinson's disease: focus on parkin. *Antioxid. Redox Signal.* **16**, 935–949 (2012).
13. Vives-Bauza, C. *et al.* Control of mitochondrial integrity in Parkinson's disease. *Prog. Brain Res.* **183**, 99–113 (2010).
14. Sharma, M. *et al.* A multicenter clinico-genetic analysis of the *VPS35* gene in Parkinson disease indicates reduced penetrance for disease-associated variants. *J. Med. Genet.* **49**, 721–726 (2012).
15. Vilariño-Güell, C. *et al. VPS35* mutations in Parkinson disease. *Am. J. Hum. Genet.* **89**, 162–167 (2011).
16. Zimprich, A. *et al.* A mutation in *VPS35*, encoding a subunit of the retromer complex, causes late-onset Parkinson disease. *Am. J. Hum. Genet.* **89**, 168–175 (2011).
17. Kumar, K.R. *et al.* Frequency of the D620N mutation in *VPS35* in Parkinson disease. *Arch. Neurol.* **69**, 1360–1364 (2012).
18. Lesage, S. *et al.* Identification of *VPS35* mutations replicated in French families with Parkinson disease. *Neurology* **78**, 1449–1450 (2012).
19. Bonifacino, J.S. & Hurley, J.H. Retromer. *Curr. Opin. Cell Biol.* **20**, 427–436 (2008).
20. Burd, C. & Cullen, P.J. Retromer: a master conductor of endosome sorting. *Cold Spring Harb. Perspect. Biol.* **6**, a016774 (2014).
21. Braschi, E. *et al.* Vps35 mediates vesicle transport between the mitochondria and peroxisomes. *Curr. Biol.* **20**, 1310–1315 (2010).
22. Soubannier, V. *et al.* A vesicular transport pathway shuttles cargo from mitochondria to lysosomes. *Curr. Biol.* **22**, 135–141 (2012).
23. Sugiura, A., McLelland, G.L., Fon, E.A. & McBride, H.M. A new pathway for mitochondrial quality control: mitochondrial-derived vesicles. *EMBO J.* **33**, 2142–2156 (2014).
24. Yoon, Y., Pitts, K.R., Dahan, S. & McNiven, M.A. A novel dynamin-like protein associates with cytoplasmic vesicles and tubules of the endoplasmic reticulum in mammalian cells. *J. Cell Biol.* **140**, 779–793 (1998).
25. Seaman, M.N. The retromer complex—endosomal protein recycling and beyond. *J. Cell Sci.* **125**, 4693–4702 (2012).
26. Cassidy-Stone, A. *et al.* Chemical inhibition of the mitochondrial division dynamin reveals its role in Bax/Bak-dependent mitochondrial outer membrane permeabilization. *Dev. Cell* **14**, 193–204 (2008).
27. Roy Chowdhury, S.K. *et al.* Impaired adenosine monophosphate–activated protein kinase signaling in dorsal root ganglia neurons is linked to mitochondrial dysfunction and peripheral neuropathy in diabetes. *Brain* **135**, 1751–1766 (2012).
28. Brand, M.D. & Nicholls, D.G. Assessing mitochondrial dysfunction in cells. *Biochem. J.* **435**, 297–312 (2011).
29. Merrill, R.A. *et al.* Mechanism of neuroprotective mitochondrial remodeling by PKA/AKAP1. *PLoS Biol.* **9**, e1000612 (2011).
30. Zhu, P.P. *et al.* Intra- and intermolecular domain interactions of the C-terminal GTPase effector domain of the multimeric dynamin-like GTPase Drp1. *J. Biol. Chem.* **279**, 35967–35974 (2004).
31. Zhao, J. *et al.* Human MIEF1 recruits Drp1 to mitochondrial outer membranes and promotes mitochondrial fusion rather than fission. *EMBO J.* **30**, 2762–2778 (2011).

© 2015 Nature America, Inc. All rights reserved.

32. Liu, T. *et al.* The mitochondrial elongation factors MIEF1 and MIEF2 exert partially distinct functions in mitochondrial dynamics. *Exp. Cell Res.* **319**, 2893–2904 (2013).
33. Lucin, K.M. *et al.* Microglial beclin 1 regulates retromer trafficking and phagocytosis, and is impaired in Alzheimer's disease. *Neuron* **79**, 873–886 (2013).
34. McLelland, G.L., Soubannier, V., Chen, C.X., McBride, H.M. & Fon, E.A. Parkin and PINK1 function in a vesicular trafficking pathway regulating mitochondrial quality control. *EMBO J.* **33**, 282–295 (2014).
35. Soubannier, V., Rippstein, P., Kaufman, B.A., Shoubridge, E.A. & McBride, H.M. Reconstitution of mitochondria-derived vesicle formation demonstrates selective enrichment of oxidized cargo. *PLoS ONE* **7**, e52830 (2012).
36. Neuspiel, M. *et al.* Cargo-selected transport from the mitochondria to peroxisomes is mediated by vesicular carriers. *Curr. Biol.* **18**, 102–108 (2008).
37. Chan, D.C. Mitochondrial fusion and fission in mammals. *Annu. Rev. Cell Dev. Biol.* **22**, 79–99 (2006).
38. Lackner, L.L. & Nunnari, J.M. The molecular mechanism and cellular functions of mitochondrial division. *Biochim. Biophys. Acta* **1792**, 1138–1144 (2009).
39. Zunino, R., Braschi, E., Xu, L. & McBride, H.M. Translocation of SenP5 from the nucleoli to the mitochondria modulates DRP1-dependent fission during mitosis. *J. Biol. Chem.* **284**, 17783–17795 (2009).
40. Tsika, E. *et al.* Parkinson's disease–linked mutations in *VPS35* induce dopaminergic neurodegeneration. *Hum. Mol. Genet.* **23**, 4621–4638 (2014).
41. McGough, I.J. *et al.* Retromer binding to FAM21 and the WASH complex is perturbed by the Parkinson disease–linked *VPS35*^{D620N} mutation. *Curr. Biol.* **24**, 1670–1676 (2014).
42. Follett, J. *et al.* The *Vps35*^{D620N} mutation linked to Parkinson's disease disrupts the cargo sorting function of retromer. *Traffic* **15**, 230–244 (2014).
43. Zavodszky, E. *et al.* Mutation in *VPS35* associated with Parkinson's disease impairs WASH complex association and inhibits autophagy. *Nat. Commun.* **5**, 3828 (2014).

© 2015 Nature America, Inc. All rights reserved.

ONLINE METHODS

Cell culture and transfection. Human neuroblastoma M17 cells were grown in Opti-MEM medium (Invitrogen), supplemented with 5% or 10% (v/v) FBS and 1% penicillin–streptomycin (P/S), in 5% CO_2 in a humid incubator at 37 °C. They were found to be free of mycoplasma contamination. Regular culture medium containing 300 μg/ml geneticin (Invitrogen) or 20 μg/ml blasticidin (Invitrogen) was used for stable–cell line selection. Three independent clones of M17 cells that stably overexpressed or were knocked down for wild-type (*VPS35*^{WT}) or mutant (*VPS35*^{R524W} and *VPS35*^{D620N}) *VPS35* were established. Primary neurons from embryonic day 18 (E18) rat cortex were isolated from rats (Harlan).

Only pregnant female rats (9–10 weeks old) were used for primary neuron isolation every other week on a continual basis under a protocol approved by the Institutional Animal Care and Use Committee (IACUC) at Case Western Reserve University. Briefly, a pregnant female rat at E18 was anesthetized and the embryos were then dissected out in dissection buffer (Hank's balanced salt solution (HBSS), 20 mM HEPES, 20 mM glucose). The heads of the embryos were removed and placed in 1.5-ml tubes containing Hibernate E (BrainBits) with 2% B27 supplement (Invitrogen). Under a dissecting microscope and in dissection buffer (Invitrogen), the skull was removed and the meninges carefully stripped away with a pair of fine forceps. The cortex of both hemispheres was dissected out after removing the hippocampus. The cortical tissue was placed in digestion solution (0.25% trypsin, 20 mM Glucose, 20 mM HEPES, DNAse 50 units/ml) for 15 min at room temperature. The activity of trypsin was stopped by adding 15% FBS in Opti-MEM. The tissue was dissociated using a 1-ml pipette by gentle trituration on the side of the tube 15 times, until no big chunks of tissue remained. The dissociated tissue was centrifuged at 200*g* for 2–3 min and the cell pellet was resuspended in day 0 culture medium (neurobasal medium, 2% B27 supplement, 1% GlutaMAX, 1% P/S (Invitrogen)). Primary neurons were seeded at 400,000 cells per coverslip (15 mm) coated with poly-L-lysine. The medium was changed the next day to culture medium without P/S. All cultures were kept at 37 °C in a humidified 5% CO_2-containing atmosphere. More than 90% of the cells were neurons after they were cultured for 7–17 d of culture *in vitro* (DIV), which was verified by positive staining for the neuronal-specific markers microtubule-associated protein (MAP) 2 (a dendritic marker) and TAU-1 (an axonal marker). At DIV 7–12, neurons were transfected using Neurofect (Genlantis) according to the manufacturer's protocol. M17 cells were transfected by Lipofectamine 2000 (Invitrogen) and the transfection efficiency was found to be almost 80%, as confirmed by immunofluorescence.

Expression vectors, antibodies, chemicals and measurement. The MitoDsRed2 (Clontech), mito-TagBFP2 (Evrogen), green fluorescent protein (GFP)-tagged wild-type *DLP1* (*DLP1*^{WT}) and dominant-negative mutant *DLP1*^{K38A} constructs were used. The expression plasmids for Flag-tagged VPS35 were constructed based on the pCMV-3Flag-1a vector (Agilent). Different mutations of *VPS35* were generated by the QuickChange Lightning kit (Agilent). The microRNA (miR) RNA interference (RNAi) vector was generated via the pcDNA 6.2-GW/EmGFP-miR construct (Invitrogen). The miR sequences targeting the different mRNA regions of exon 5 in the open reading frame regions of the human, rat and mouse *Vps35* were: 5′-TCGCTTCACACTGCCACCTTT-3′ (#1) and 5′-TTCACACTGCCACCTTTGGTA-3′ (#2). The predesigned Vps26-specific siRNA sequence is: 5′-GCCUUACCUGGAGAACUCAtt-3′ (Invitrogen). Primary antibodies used include mouse anti-DLP1 (BD Biosciences, catalog number 611112, 1:5,000 dilution), mouse anti-Mfn1 (Santa Cruz, catalog number sc-50330, 1:2,000 dilution), anti-Mfn2 (Santa Cruz, catalog number sc-100560, 1:2,000 dilution), mouse anti-NeuN (Millipore, catalog number MAB377, 1:300 dilution), mouse anti–β-actin (Chemicon, catalog number MAB1501, 1:10,000 dilution), rabbit anti–β-III-tubulin (Cell Signaling, catalog number 2125, 1:300 dilution), rabbit anti-DLP1 (Cell Signaling, catalog number 8570, 1:50 dilution), mouse anti–α-tubulin (Cell Signaling, catalog number 3873, 1:300 dilution), mouse anti-Tom20 (BD Biosciences, catalog number 612278, 1:2,000 dilution), mouse OXPHOS cocktail (Abcam, catalog number ab110411, 1:2,000 dilution), mouse anti-COX IV (Cell Signaling, catalog number 4850, 1:5,000 dilution), mouse anti-Flag (Cell Signaling, catalog number 8146, 1:10,000 dilution), rabbit anti-VPS35 (Epitomics, catalog number 7514-1, 1:2,000 dilution), rabbit anti-VPS26 (Abcam, catalog number ab23892, 1:2,000 dilution), rabbit anti–tyrosine hydroxylase (Abcam, catalog number Ab112, 1:300 dilution), rabbit anti-PEX19 (Pierce, catalog number PA5-22129, 1:300 dilution). DLP1 inhibitor mdivi-1 was obtained from Enzo and hydrogen peroxide (H_2O_2), paraquat dichloride, *N*-acetylcysteine and bafilomycin A1 were obtained from Sigma. Dithiobismaleimidoethane (DTME) was from Pierce. Cell death in M17 cells was measured by the Cytotoxicity Detection Kit (LDH; Roche). ATP levels were measured by the ATP Colorimetric-Fluorometric Assay Kit (Biovision). The ROS level and mitochondrial membrane potential were measured as described before[4]. The propidium iodide assay for neuronal viability of cultured primary neurons was performed as described previously[44].

Lentivirus production, stereotaxic injection and cryosectioning. Mouse surgery and procedures were performed according to NIH guidelines and were approved by the Institutional Animal Care and Use Committee (IACUC) at Case Western Reserve University. A minimal number of mice was used (n = 3 or 4 per group). 2- to 3-month-old FVB (n = 3 per group) or C57BL/6J mice (n = 4 per group), both male and female, were randomly assigned to receive different injections. Lentivirus expression plasmids were constructed by inserting the *VPS35*-p2a-mitoDsRed2 fragment (Addgene) into pLVX-Puro vector from Clontech. Lenti-X 293T cells (Clontech) were transfected with the expression plasmids and two helper plasmids (Addgene; Δ8.2 and vesicular stomatitis virus G protein) at 6 μg, 4.5 μg and 1.5 μg of DNA per 10-cm plate using PerFectin (Genlantis). 48 h after transfection, the supernatants of eight plates were pooled, centrifuged at 780*g* for 30 min and filtered (0.45-μm pore size). The supernatants were laid on the top of 20% sucrose in PBS and centrifuged in a Beckman SW-28 rotor at 110,000*g* for 2 h. The pellet was resuspended in 100 μl of PBS. Mice were anesthetized using avertin at 2.5% (v/v) and placed in a stereotactic frame. A small incision was made to expose the skull surface and to visualize the bregma. Holes were drilled in the skull overlying the ventral tegmental area (VTA) (anteroposterior (AP) −3.3 mm, medial-lateral (ML) −0.8 mm, dorsal-ventral (DV) −4.6 mm) and a 10-μl microsyringe (Hamilton) was filled with virus. The needle was lowered down 4.6 mm from the bregma, 1 μl of virus (109 viral particles/ml) was injected within 5 min and the needle was left in place for 5 min before slowly withdrawing it. The skin was sutured and mice were allowed to recover. Three weeks after virus injection, mice were deeply anesthetized with avertin and transcardially perfused with cold PBS. The brain was dissected out and immersion-fixed in paraformaldehyde for 24 h and then in 30% sucrose for 24 h. After cryoprotection, the brain was frozen in −80 °C and 20-μm coronal sections were cut. Three serial sections around the virus injection site, which covers the substantia nigra region, were immunostained with anti-TH antibody and anti-NeuN antibody. The numbers of TH-positive and TH-negative neurons were identified using ImageJ software (developed by W. Rasband) and the percentage of neuronal loss was calculated and averaged by comparing the neuronal number between the virus-injected side and the non-injected side, and normalized to the mice injected with vector-only construct. The outcomes were independently assessed by an investigator who was blinded to the treatments.

Western blot and immunoprecipitation. Cells were lysed with 1× Cell Lysis Buffer (Cell Signaling) or radio-immunoprecipitation assay (RIPA) buffer (Sigma), plus 1 mM phenylmethylsulfonyl fluoride (Sigma) and protease inhibitor cocktail (Sigma). Equal amounts of total protein extract (5 or 20 μg) were resolved by SDS-PAGE and transferred to Immobilon-P membrane (Millipore). After blocking with 10% nonfat dry milk, primary and secondary antibodies were applied, and the blots were developed with the Immobilon western chemiluminescent horseradish peroxidase (HRP) substrate (Millipore). Immunoprecipitation was performed with antibodies against DLP1, Flag or VPS35 in RIPA buffer using the Dynabeads Protein G-IP Kit (Invitrogen) and analyzed by western blot.

Human brain samples. Frozen samples of the substantia nigra from the brains of individuals with PD (n = 5, ages = 75–88 years, postmortem interval = 5.5–18.8 h) and gender- and age-matched controls (n = 5, ages = 77–86 years, postmortem interval = 3–19 h) were obtained from the Harvard Brain Tissue Resource Center, NIH Neurobiobank and Case Western Reserve Brain Bank under protocols approved by the Institutional Review Board for Human Investigation

© 2015 Nature America, Inc. All rights reserved.

at Case Western Reserve University. Tissues were homogenized in RIPA buffer and centrifuged at 18,000*g* for 15 min at 4 °C. Equal amounts of protein extracts were used for immunoprecipitation using immobilized anti-DLP1 antibody.

Mitochondria isolation. Crude preparations and purified mitochondria were isolated as described[5] with modification. Briefly, cells were trypsinized, washed in PBS and resuspended in a minimal volume of IB-1 solution (225 mM mannitol, 75 mM sucrose, 0.1 mM EGTA, 20 mM HEPES, pH 7.4). The cells were homogenized until ~80% of the cells were lyzed, and the lysate was centrifuged at 600*g* for 5 min to remove nuclear contaminants and unbroken cells. The supernatant was once again centrifuged at 600*g* for 5 min, followed by a centrifugation at 7,000*g* for 10 min to isolate mitochondria. The supernatant was collected as the cytosolic fraction. The mitochondrial pellet was washed in 20 ml IB-2 solution (225 mM mannitol, 75 mM sucrose, 20mM HEPES, pH 7.4), centrifuged at 7,000*g* for 10 min, resuspended in 20 ml IB-2 solution, centrifuged at 10,000*g* for 10 min and finally resuspended in 2 ml MRB buffer (250 mM mannitol, 5 mM HEPES, 0.5 mM EGTA, pH 7.4) to make crude mitochondria. The crude mitochondrial fraction was overlaid on top of 8 ml Percoll medium (225 mM mannitol, 25 mM HEPES pH 7.4, 1 mM EGTA and 30% Percoll (v/v)). MRB buffer was added on top of the mitochondrial layer, followed by centrifugation at 95,000*g* in a SW40 rotor for 30 min at 4 °C. The purified mitochondrial fraction was collected and resuspended in 20 ml MRB buffer and centrifuged 10 min at 6,300*g*. The pellet was resuspended in 1 ml MRB buffer and centrifuged at 6,300*g* in an Eppendorf microcentifuge for 2 min. Isolated mitochondria were lysed with Cell Lysis Buffer (Cell Signaling) or RIPA buffer and were then analyzed by direct western blot analysis or immunoprecipitation.

Live-cell cross-linking. M17 cells were seeded into the 6-well plate for 24 h. After a wash with PBS, cells were incubated with HBSS containing 0.5 mM dithiobismaleimidoethane (DTME, from freshly prepared stocks in DMSO) for 5 min or Opti-MEM culture medium containing 0.25 mM disuccinimidyl suberate (DSS, from freshly prepared stocks in DMSO) for 30 min at 37 °C. The HBSS-DTME or Opti-MEM–DSS was removed and the mitochondrial fraction was isolated. For DTME cross-linking, mitochondria were lysed in buffer containing 60 mM Tris pH 6.8 and 0.2% SDS. Insoluble debris was removed by centrifugation (10 min at 14,000*g*) and cleared lysates were layered onto 1 ml of a 300-mM sucrose cushion and subjected to ultracentrifugation (30 min at 270,000*g*). These 270K pellets were dissolved in SDS sample buffer containing 5% β-mercaptoethanol to cleave the cross-linker and were analyzed by SDS-PAGE. For DSS cross-linking, mitochondria were lysed in Cell Lysis Buffer and directly subjected to SDS-PAGE.

Immunofluorescence, fluorescence recovery after photobleaching (FRAP) and time-lapse imaging. For immunofluorescence, neuronal cells cultured on 4- or 8-well chamber slides were fixed and stained. All fluorescence images were captured at room temperature with a Zeiss LSM 510 inverted laser-scanning confocal fluorescence microscope (controlled through Zeiss LSM 510 confocal software, Zeiss) equipped with an Alpha-Plan Fluor 100× numerical aperture (NA) 1.45 oil objective (working distance: 0.11 mm; Zeiss). Confocal images of far-red fluorescence were collected using 633-nm excitation light from a helium-neon (HeNe) laser and a 650-nm long-pass filter; images of red fluorescence were collected using 543-nm excitation light from an argon laser and a 560-nm long-pass filter; and green fluorescence images were collected using 488-nm excitation light from an argon laser and a 500- to 550-nm bandpass barrier filter. For fluorescence recovery after photobleaching (FRAP), M17 cells were seeded on glass-bottom microwell dishes (MaTek) for 24 h and then transfected with mitoDsRed2 and GFP–DLP1 plasmids. Using the 488 nm laser line of a Zeiss LSM 510 confocal microscope, GFP–DLP1 fluorescence of a selected region was bleached and fluorescence recovery was tracked by capturing images every 5 s for 5 min. Image stacks were analyzed, and the recovery curves were normalized to pre-bleach intensity and corrected for acquisition bleach by ImageJ. Time-lapse tracking of DLP1 and VPS35 was imaged by a spinning-disk confocal microscope (PerkinElmer) using a 63× objective. Frames were captured every 3 s for 10 min in a well-equipped environmental chamber with controlled CO_2 content, humidity and temperature, and imaged at 37 °C.

Image analysis. Image analysis was performed with open-source image-analysis programs WCIF ImageJ (developed by W. Rasband). Mitochondrial morphology was quantified as previously described[44]. Taken briefly, raw images were background-corrected, linearly contrast-optimized, applied with a 7 × 7 'top hat' filter, subjected to a 3 × 3 median filter and then thresholded to generate binary images. Most mitochondria were well separated in binary images and large clusters of mitochondria were excluded automatically. All binary images were analyzed by ImageJ to provide information about mitochondrial aspect ratio (ratio between major and minor axes of an ellipse equivalent to the mitochondrion as an index for mitochondrial morphology). The researchers counting mitochondria abnormalities or cell death were all blinded to the identity of the experiment.

Yeast two-hybrid analyses. Yeast two-hybrid experiments were performed using the Matchmaker GAL4 Two-Hybrid (Clontech) System 3 with vectors pGBKT7 and pGADT7, which contain the binding domain and activation domain, respectively. Yeast strain AH109 (Clontech) was transformed with empty pGBKT7 and pGADT7 vectors or pGBKT7 and pGADT7 vectors encoding DLP1 or VPS35 using Yeast Transformation Kit (Clontech). After transformation, yeast cells were plated on synthetic defined (SD) medium lacking leucine and tryptophan, and colonies were then by streaked onto high-stringency plates (SD –Leu –Trp –His –Ade). β-galactosidase activity in different yeast clones was measured by Yeast β-Galactosidase Assay Kit (Piercenet) following the manufacturer's instructions.

Human fibroblasts. Primary human fibroblast from a PD patient with the *VPS35*^{D620N} mutation was generated and characterized as previously published[41]: Briefly, two 2-mm^2 skin biopsies were taken from the forearms of a healthy donor patient and a Parkinson's disease patient genotyped to harbor the *VPS35*^{D620N} mutation. These were each placed into a sterile sample tube (Sterilin, UK) along with 10 ml of fibroblast medium (Dulbecco's Modified Eagle's Medium (DMEM), Sigma D6546) before transportation to the lab on wet ice (total time <30 min). The epidermis and any fat were removed (sterile scalpel and forceps) before cutting into four roughly equal pieces, which were placed into a 4-well plate (Nunc) pre-coated with CELLstart (1:200 in PBS(+/+), Sigma D8662) in 200 µl of fibroblast media supplemented with 10% heat-inactivated fetal bovine serum, (Invitrogen, 10500), 1% GlutaMAX (Invitrogen, 35050), 1% non-essential amino acids (NEAA; Invitrogen, 11140), 1% penicillin-streptomycin (Sigma, P4458)). Cultures were left for up to 2 weeks to allow cell attachment to the matrix and dermal fibroblast proliferation. At 80% confluency cells were enzymatically passaged using TrypLE Express (Gibco, 12604) and passaged at a ratio of 1:3 until cryopreservation.

Primary human fibroblasts from four gender- and age-matched normal subjects (normal human fibroblasts, NHFs) were obtained from Coriell Institute for Medical Research.

Primary fibroblasts were grown in minimum essential medium (Invitrogen) containing non-essential amino acids and 2 mM glutamine, supplemented with 10% or 15% (v/v) fetal bovine serum, in 5% CO2 in a humid incubator at 37 °C. Fibroblasts cells were transfected with Effectene Transfection Reagent (Qiagen) according to the manufacturer's protocol and imaged as we previously reported[45].

***In vitro* reconstitution of MDVs.** Mitochondrial-budding assay was performed as previously reported[35] with minor modification. Briefly, isolated mitochondria from mouse liver were washed three times and then resuspended in the mitochondria resuspending buffer (250 mM mannitol, 5 mM HEPES, 0.5 mM EGTA, pH 7.4). M17 cells were seeded in the 10-cm dish, and cells were harvested after trypsinization. Cells were homogenized in IB-1 buffer (IB-1: 225 mM manitol, 75 mM sucrose, 0.1 mM EGTA, 20 mM HEPES, pH 7.4) and cytosolic fractions were prepared by centrifugation at 180,000*g* for 30 min. Cytosolic fractions for each cell line were aliquoted and stored in −80 °C. For budding assay, mitochondria (1 mg) were incubated with or without cell cytosol fraction (200 µg) at room temperature in a final 100-µl system with the following reagents: 225 mM mannitol, 75 mM sucrose, 80 mM KCl, 0.1 mM EGTA, 20 mM HEPES, 1.6 mM $MgCl_2$, 1.6 mM ATP, 5 mM succinate, 2 mM K_2HPO_4, 0.3 mM phosphocreatine, 8.3 mg/ml creatine phosphokinase, pH 7.4). In a control experiment, 10 mM

© 2015 Nature America, Inc. All rights reserved.

doi:10.1038/nm.3983

N-ethylmaleimide (NEM, Sigma) was added to the reaction to inhibit the budding process. After the reaction, mitochondria were removed by centrifugation at 10,000*g* and the supernatant fraction was further treated with 0.25% trypsin for 5 min at room temperature. Then samples were lysed by 10× cell lysis buffer for western blot.

Transmission electron microscopy (TEM) and Immuno-electron microscopy (IEM). For TEM, fibroblasts were seeded onto a sterilized Aclar Embedding Film (Electron Microscopy Sciences, PA), lining the wells in a 6-well cell culture cluster. After the cells had reached ~80% of confluence, the Aclar sheets with their attached cells were immersed in fixative. The initial fixative was 0.25% glutaraldehyde in cacodylate buffer (Electron Microscopy Sciences, PA) (pH 7.3). The specimen was post-fixed in ferrocyanide-reduced 1% osmium tetroxide (Electron Microscopy Sciences, PA). The samples were processed as previously reported[46].

An aliquot of isolated mitochondrial suspension prepared from mouse liver was added to an equal volume of half half-strength Karnovsky's fixative (Electron Microscopy Sciences, PA) and immediately spun down in a microcentrifuge (4,000*g*). The resulting pellet was transferred to fresh quarter-strength Karnovsky's fixative. After a rinse in buffer, the pellet was post-fixed in ferrocyanide-reduced osmium tetroxide, then rinsed in distilled water. The pellet was soaked overnight in acidified 0.25% uranyl acetate, and embedded in Poly/Bed 812 (Polysciences, Inc., PA), then examined in a JEOL 1200EX electron microscope, Zeiss CEM 902 Electron microscope, and FEI Tecnai Spirit (T12) with a Gatan US4000 4k × 4k charged-coupled device (CCD).

For IEM, isolated mitochondria prepared from mouse liver were fixed in 4% w/v formaldehyde containing 0.1% w/v glutaraldehyde in 0.1 M HEPES buffer (Electron Microscopy Sciences, Hatfield, PA) at room temperature for 45 min, then dehydrated in ethanol and embedded in LR White resin (Polysciences, Inc., Warrington, PA). Immuno-gold labeling procedure was performed according to the method described by Fujioka *et al.*[47]. Thin sections were blocked with PBS containing 1% w/v BSA, 1% v/v normal goat serum and 0.01% v/v Tween 20 (PBGT). Grids were then incubated with mouse anti-DLP1 antibody at a 1:8 dilution in PBGT for 12 h at 4 °C. Negative controls included normal mouse serum and PBT in place of the primary antibody. After washing, grids were incubated for 1 h in 10 nm gold-conjugated goat anti–mouse IgG (British BioCell International, Ted Pella, Inc., Redding, CA) diluted 1:30 in PBGT, rinsed with PBS, and fixed with glutaraldehyde to stabilize the gold particles[47]. Gold-labeled thin sections were stained first with 2% uranyl acetate in 50% methyl alcohol acidified uranyl acetate at 38 °C for 30 min, then with the triple-lead stain of Sato as modified by Hanaichi *et al.*[48] and then examined in a JEOL 1200EX electron microscope, Zeiss CEM 902 Electron microscope, and FEI Tecnai Spirit (T12) with a Gatan US4000 4k × 4k CCD.

Seahorse XF24 mito-stress analysis. M17 neuroblastoma cells were cultured in Seahorse XF-24 (Seahorse Bioscience, Billerica, USA) plates which were coated with poly-D-lysine (50 μg/ml). M17 cells were seeded at a density of 100,000 cells per well. For primary fibroblasts, cells were seeded at a density of 50,000 cells per well. Before assay, culture medium was changed to unbuffered DMEM (DMEM base medium supplemented with 25 mM glucose, 1 mM sodium pyruvate and 1 mM GlutaMAX) and cells were incubated at 37 °C in a non-CO_2 incubator for 45 min. The assay protocol consisted of repeated cycles of 3 min mixing, 2 min wait and 3 min measurement periods. Basal oxygen consumption rate (OCR) was measured three times before drug exposure. Then oligomycin (1 μM) (Seahorse Bioscience), carbonyl cyanide-4-(trifluoromethoxy)phenylhydrazone (FCCP) (0.5 μM for M17 cells and 2 μM for primary fibroblasts) (Seahorse Bioscience) and rotenone and antimycin A (0.5 μM) (Seahorse Bioscience) were injected sequentially into the medium in each well. After injection of each drug, OCR measurements were made three times. After the assays, protein concentrations for each well were measured to confirm that similar cell numbers were seeded.

Fatty acid translocase (FAT or CD36) receptor recycling assay. Receptor recycling assays were performed as previously described[33] with minor modification. M17 cells in which *VPS35* was knocked down (*VPS35*^{KD} M17 cells) were seeded in 4-well glass chamber slide at a density of 100,000 cells per well in 5% FBS of Opti-MEM. Cells were transfected with plasmids containing *VPS35* mutations for 72 h. Culture medium was changed to Opti-MEM with 10% FBS for 2 h at 37 °C, then cells were incubated in Opti-MEM (1% FBS) with antibody against FAT (CD36) (Santa Cruz) for 1 h at 37 °C. Cells were acid-washed with cold Opti-MEM (pH 2.0) and then were cultured in Opti-MEM with 10% FBS for another 1 h at 37 °C. Then cells were incubated in Opti-MEM (1% FBS) with Alexa Fluor 568–conjugated anti-rabbit antibody for 1 h at 37 °C. Cells were again acid-washed with cold Opti-MEM at pH 2.0. Cells were then fixed with 4% paraformaldehyde for 15 min and were permeabilized with 0.5% Triton X-100 for 40 min. Transfected cells were identified by anti-Flag staining and nuclei were stained by DAPI. Recycled fluorescent signal were analyzed by ImageJ. Briefly, image background was subtracted by the rolling-ball radius method and was then thresholded. Averaged thresholded fluorescent signal area was obtained for cells.

Statistical analysis. Our power analysis indicated that to detect 20% difference at $\alpha = 0.05$ and $\beta = 0.8$, with <0.05 probability of false errors using the typical variances we have in our data requires a minimum of 12 samples. No samples were excluded. Data were normally distributed with similar variances between the groups. All of the outcomes were independently assessed by an investigator who was blinded to the treatments. Data are means ± s.e.m. from three independent experiments. Statistical analysis was done with one-way analysis of variance (ANOVA) followed by Tukey's multiple-comparison test. *n* represents the number of neurons analyzed. $P < 0.05$ was considered to be statistically significant; n.s., not significant.

44. Wang, X. *et al.* Impaired balance of mitochondrial fission and fusion in Alzheimer's disease. *J. Neurosci.* **29**, 9090–9103 (2009).
45. Wang, X., Su, B., Fujioka, H. & Zhu, X. Dynamin-like protein 1 reduction underlies mitochondrial morphology and distribution abnormalities in fibroblasts from sporadic Alzheimer's disease patients. *Am. J. Pathol.* **173**, 470–482 (2008).
46. Fujioka, H., Tandler, B., Consolo, M.C. & Karnik, P. Division of mitochondria in cultured human fibroblasts. *Microsc. Res. Tech.* **76**, 1213–1216 (2013).
47. Fujioka, H. *et al.* Decreased cytochrome c oxidase subunit VIIa in aged rat heart mitochondria: immunocytochemistry. *Anat. Rec. (Hoboken)* **294**, 1825–1833 (2011).
48. Hanaichi, T. *et al.* A stable lead by modification of Sato's method. *J. Electron Microsc. (Tokyo)* **35**, 304–306 (1986).

© 2015 Nature America, Inc. All rights reserved.